Multi-Analyte Detection Based on Integrated Internal and External Sensing Approach

Firoz Haider, Md. Mashrafi, Rifat Ahmmed Aoni, Rakib Haider, Moqbull Hossen, Tanvir Ahmed, Ghafour Amouzad Mahdiraji, and Rajib Ahmed

Abstract—Highly sensitive, simple and multiplex detection capabilities are key criteria of point-of-care (POC) diagnosis in clinical samples. Here, a simple and highly sensitive multi-analyte detection technique is proposed by using photonic crystal fiber (PCF) based surface plasmon resonance (SPR) sensor that employs both internal and external sensing approaches. The proposed sensor can detect two different analytes simultaneously by the internal and external plasmonic micro-channels. The light propagation through the sensor is controlled by the scaled-down air-holes to excite the free electrons of the plasmonic metal layers. The light-guiding and sensing properties of the sensor is numerically analyzed by using the Finite Element Method (FEM). The proposed sensor shows the maximum wavelength sensitivities (WS) of 12,000 nm/refractive index unit (RIU), and 10,000 nm/RIU, for the internal and external sensing approaches, respectively, and corresponding resolution of 8.33×10^{-6} RIU and 1.0×10^{-5} RIU. Moreover, the hybrid sensor is applicable to detect unknown analyte refractive index (RI) in the range of 1.33 to 1.40 which covers extensively investigating analytes such as viruses, different cancer cells, glucose, proteins and DNA/RNA. Due to high sensing performance with multi-analyte detection capability, the proposed sensor can play a significant role to detect bio targets at the POC platform.

Index Terms—photonic crystal fiber, surface plasmon resonance, optical fiber sensors and finite element method.

F. Haider is with the School of Engineering, Taylor's University, Subang Jaya, Selangor, 47500, Malaysia (e-mail: firozhaider@sd.taylors.edu.my).

M. Mashrafi is with Department of Electrical and Electronic Engineering, University of Dhaka, 1000, Dhaka, Bangladesh (e-mail: mdmashrafi9@gmail.com).

A. A. Rifat is with the Department of Electronic Materials Engineering, Australian National University, Acton, ACT-2601, Australia (e-mail: RifatAhmmed.Aoni@anu.edu.au).

R. Haider with the Department of Electrical and Electronic Engineering, Daffodil international university, 1207, Dhaka, Bangladesh (e-mail:haideurakib@gmail.com).

M. Hossen is with the School of Computing and Engineering, University of Missouri-Kansas City, Kansas City, MO 64110, USA (e-mail: mmhpn6@mail.umkc.edu)

T. Ahmed is with the Department of Electrical and Electronic Engineering, Rajshahi University of Engineering & Technology, Bangladesh (e-mail: tanvir_eee_ruet@yahoo.com).

G. Amouzad Mahdiraji is with Flexilicate Sdn. Bhd., University of Malaya, Kuala Lumpur, 50603, Malaysia (e-mail: ghafouram@gmail.com).

R. Ahmed is with the School of Medicine, Stanford University, Palo Alto, CA 94304, USA (e-mail: rajibah@stanford.edu).

I. Introduction

TO date, a lot of research works have been reported based on PCF-based SPR sensing technique. PCF-based SPR sensors are commonly used in different sort of sensing applications such as chemical, biological, food, and biochemical sensing [1-5]. The key advantages of using PCF-SPR sensors are considered for wide range of detection, controllable dispersion, a high degree of integration, better line confinement, small in size, and highly sensitive characteristics [6-8]. The sensitivity of a PCF SPR sensor strongly relies on plasmonic materials such as gold, silver, copper, aluminium, palladium, and bismuth. The gold (Au) shows strong chemical stability and a broad shift of resonant peak compared to other plasmonic materials [9-11]. Until now, most of the reported PCF SPR sensors are limited to single analyte detection [6, 9, 12]. Recently, Ayyanar *et al.* has been reported a D-shaped PCF sensor for single analyte detection with a sensing layer of Au/Ge2Sb2Te5 and shows maximum WS of 17,600 nm/RIU (crystalline phase) and 8,000 nm/RIU (amorphous phase) [1]. By internal sensing approach, Dash *et al.* has been introduced a biosensor for single analyte detection with maximum WS of 2,000 nm/RIU in the sensing RI range of 1.33 to 1.35 [13]. An external sensing approached based PCF sensor is proposed by Jahan et al. with the maximum sensitivities of 20,000 nm/RIU in wavelength and 1380 RIU^{-1} in amplitude [14]. Though, the sensor has shown good performance but limit to single analyte detection. Recently, a few numbers of PCF-based SPR sensors have been reported for multi-analyte detection based on either internal or external sensing approaches [2, 15, 16]. In our previous work, we have shown that internally coated grapefruit PCF can be used to detect three different analytes simultaneously and achieved the maximum WS of 2,000 nm/RIU (1st channel), 3,000 nm/RIU (2nd channel), and 18,000 nm/RIU (3rd channel) [2]. Also, Kaur *et al. has* proposed a biosensor with two sensing layers that shows maximum WS of 1,000 and 3,750 nm/RIU [17]. Besides, a multi-analyte detection-based PCF SPR is proposed based on an external sensing approach which exhibits the maximum WS of 2,500 nm/RIU (Ch-1) and 3,083 nm/RIU (Ch-2), respectively in the *x*- and *y*-polarized modes [15]. Also, Otupiri *et. al* introduced a micro-slotted-based PCF sensor for multi-analyte detection that exhibited maximum WS of 4,600 nm/RIU (x-polarized mode) and 2,300 nm/RIU (y-polarized mode), respectively [18]. All the reported multi-analyte detection-based sensors are designed by either the internal or external sensing approaches. In the internal sensing approach, the internal surface of selective holes (usually the diameter is few nm to 1-2 μm) needs to coat with the plasmonic materials.

Additionally, the liquid needs to infiltrate to the selective air holes, which makes this approach very complex in terms of fabrication. On the other hand, external sensing approach overcomes the complexity of the internal sensing approach as all the metallic coating and analyte infiltration can be applied externally. However, external sensing approach sometimes show very low sensitivity due to the long distance between the core and the metallic layer. Therefore, an intense investigation is highly recommended to develop a multianalyte detection technique with a hybrid (internal and external) biosensing approach. In addition, the multi-analyte sensing approach offers fast detection, accurate, and cost-effective facilities [16, 19].

In this work, a simple hybrid biosensing approach is introduced by combining internal and external sensing to detect multi-analytes. The hybrid PCF SPR sensing approach can be a solution of internal and external sensing approach separately. The sensor will reduce the liquid infiltration, metal coating complexity and low sensitivity problem by offering the large internal channel (diameter 4.4 µm) and placing the core near to the external sensing channel. The internal and external channels in the PCF are excited by propagating light which passes through the linear scaled-down air-holes and shows improvement in RI sensing. The hybrid sensor can be applied to detect unknown analyte RI in the range of 1.33 to 1.41 with high accuracy in both channels. Moreover, structural parameters of the sensor such as pitch size, diameter of different air-holes, and thickness of gold layer are optimized to acquire the maximum sensing performance and accurate multiplex analyte detection, which may be suitable for POC diagnosis at resource-limits-settings.
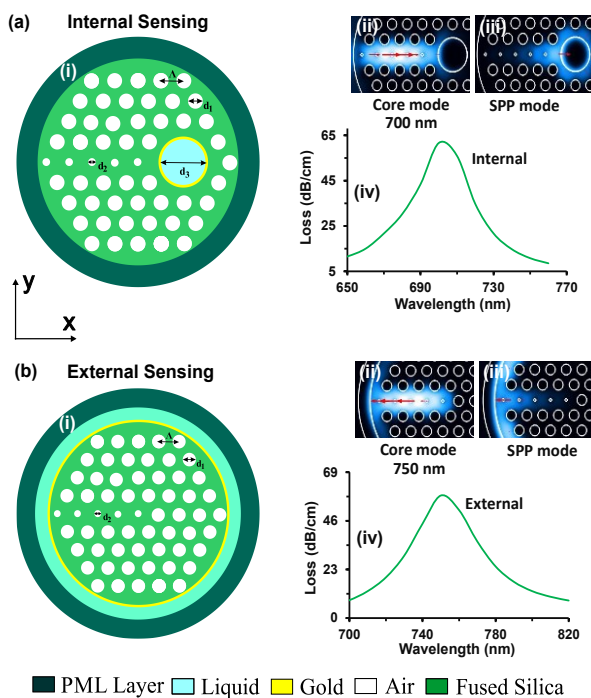

Fig. 1. Cross-section view of the a(i) internal sensing, b(i) external sensing, a(ii-iii) and b(ii-iii) corresponding electric field distribution of core mode and SPP mode, respectively and a(iv) and b(iv) shows the loss spectrum at analyte RI of 1.38.
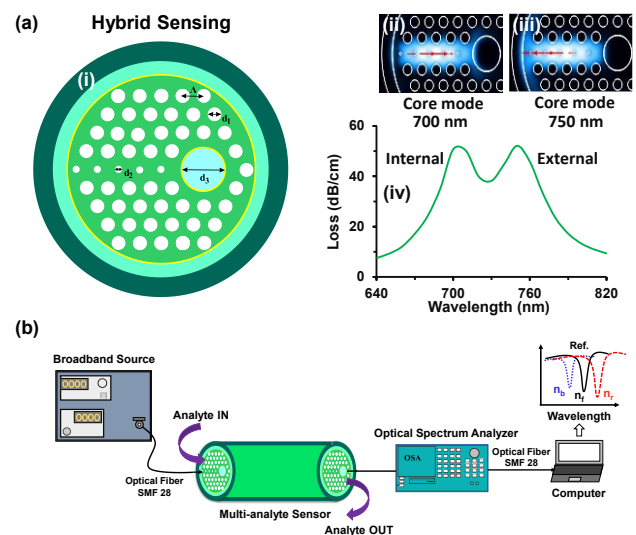

Fig. 2. Cross-section view of the a(i) hybrid sensing approach, a(ii-iii), corresponding electric field distribution of core mode at 700 nm and 750 nm respectively for internals and externals, a(iv) loss spectrum at analyte RI of 1.38 for hybrid sensing approach and (b) schematic experimental-set up of the hybrid sensor.

II. STRUCTURAL DESIGN AND METHODS

Figs. 1 a(i) and b(i) show the conventional internal and external sensing approaches. Corresponding field distribution of core and SPP modes are shown in Figs. a(ii-iii) and b(ii-iii), respectively. Figs. 1 a(iv) and b(iv) show the different resonant peaks at 700 nm and 750 nm for internal and external sensing approaches, respectively at analyte RI of 1.38. In Fig. 2 a(i), a hybrid structure is proposed by combining internal and external sensing approaches. From the Figs. a(ii-iv), it seems that the proposed hybrid structure shows similar characteristics (core light interaction) at analyte RI of 1.38 as like internal and external sensing approaches. Moreover, confinement loss decrease (52 dB/cm) and resonant peaks appear at the same wavelengths (700 nm and 750 nm) for the proposed hybrid sensor. Furthermore, we have considered the same parameters for all the structures and cladding consists of four hexagonal air-hole rings. Five scaled-down air holes are used to form a core that leads the propagating light to excite surface plasmon waves in both channels with a high coupling intensity. Also, scaled-down air holes are used to regulate the direction of light propagation for better light confinement [12]. The regular air-holes diameter of d_1=1.4 µm is considered to form the fiber cladding and the diameter of scaled-down air-holes is d_2=0.35 µm. A large internal sensing channel is introduced with an air hole diameter of d_3=4.4 µm by removing seven air holes from the right side of the scaled-down air holes. Pitch size is kept at Λ=2.3 µm to stimulate the evanescent field. The considered gold layer thickness is t_g=40 nm in both channels. Fused silica usually consider as a primary material of PCF fiber and the RI is obtained by the Sellmeier equation [20, 21].

$$n^2(\lambda) = 1 + \frac{B_1 \lambda^2}{\lambda^2 - C_1} + \frac{B_2 \lambda^2}{\lambda^2 - C_2} + \frac{B_3 \lambda^2}{\lambda^2 - C_3} \qquad (1)$$

where n defines the RI of silica, λ is the wavelength of incident light in micrometer unit and other Sellmeier constants are taken from [22]. Plasmonic material gold has a significant impact on the sensitivity of a sensor. The permittivity of gold can be obtained by using the Drude-Lorentz model [23];

$$\varepsilon_{Au} = \varepsilon_{\infty} - \frac{\omega^2{}_D}{\omega(\omega + j\gamma_D)} - \frac{\Delta\varepsilon.\Omega^2{}_L}{(\omega^2 - \Omega^2{}_L) + j\Gamma_L\omega} \quad (2)$$

Where ε_{AU} is the permittivity of gold and the value of constant co efficient can be obtained from [3]. The sensor performances are explored through the FEM-based software COMSOL Multiphysics. A perfectly matched layer (PML) and the scattering boundary conditions are applied to absorb the reflection of light from the boundary [24]. The proposed PCF design can be fabricated by the standard stack-and-draw method [25]. A set of capillaries with the diameter of 1.25 mm can be used and stacked inside the hexagonal jigs to achieve the hexagonal PCF preform. By utilizing the thin and thicker wall capillaries, the regular air holes, scaled-down air-holes and larger air-holes can be achieved [2, 26]. Another way to control the air-holes sizes are employing self-pressurization during the fibre fabrication. In this process, one end of an intended air holes will be sealed with the glue under the microscope. By applying pressure or suck from the other side it is possible to achieve large or small air-holes, respectively. The drawing temperature is another key parameter that has significant influence in controlling the air-holes sizes. After the PCF fabrication, the plasmonic material gold needs to deposit on the surface of the internal and external sensing channel. The chemical vapor deposition (CVD) or atomic layer deposition (ALD) method can be applied for the gold layer deposition [7, 27]. To realize the real-time experiment process, a schematic of the physical experimental set-up is presented in Fig. 2(b). A broadband light source can be used along with lens, polarizer, optical shutter and objective to propagate polarized light at certain acceptance angle to couple light through the PCF core that will excite the respective analyte channels. The liquid can be infiltrated to the channels via inlet through a syringe pump (withdraw/injection mode) and outlet for changing analyte liquid. The optical spectrum analyzer (OSA) will be used to detect the resonance spectrum shift. The spectrum resonance will show either blue shift or read shift with the change of analyte RI.

III. RESULTS AND ANALYSIS

The operating mechanism of the PCF-SPR sensor is highly dependent on the interaction of the evanescent field with surface electrons of the plasmonic material. The evanescent field originates from the light wave propagation in the PCF core. A surface plasmon wave (SPW) is produced while the evanescent field stimulates the free electrons of the metal surface. The phase-matching condition occurs when the propagation constant of SPP mode and core mode are completely matched. Due to the sensitive nature of SPP mode on the RI of the analyte, a significant change in phase matching condition occurs depending on the change in analyte RI. At the phase-matching condition, a sharp propagation loss

peak occurs. When a small change occurs in the analyte RI, it produces a significant change in the loss characteristics [28, 29]. By observing the resonant peak shift or confinement loss variation, an unknown analytes RI can be detected. The propagation loss is calculated using the following equation [24];

$$\alpha(dB/cm) = 8.686 \times k_0 \, Im(n_{eff}) \times 10^4 \quad (3)$$

where λ indicates the operating wavelength, $Im(n_{eff})$ is the imaginary part of the refractive index of the core mode. The effective index of core-guided mode and SPP mode are varied with the small variation of analyte RI. To demonstrate the multi-analyte sensing phenomena, the sensing range is divided into two groups such as lower analyte RI (from 1.33 to 1.36) and higher analyte RI (from 1.37 to 1.41). Here are some real-life examples of biomolecules with their corresponding RI values which can be detected with our proposed sensor such as 5% saline solution (RI=1.342), milk (RI=1.35), Ethanol (RI=1.36), 6.8% nucleoid mainly with DNA solution in water (RI=1.371), 21% protein solution (RI=1.39) and 0.5% cytoplasm with RNA solution (RI=1.39) [30-33]. Furthermore, the sensor performance is analyzed by two sensing schemes. In sensing Scheme-I, higher RI analyte flows through the external channel and lower RI analyte infiltrates into the internal channel. Besides, in sensing scheme-II, the external channel is associated with a lower RI analyte whereas a higher RI analyte penetrates the internal channel.
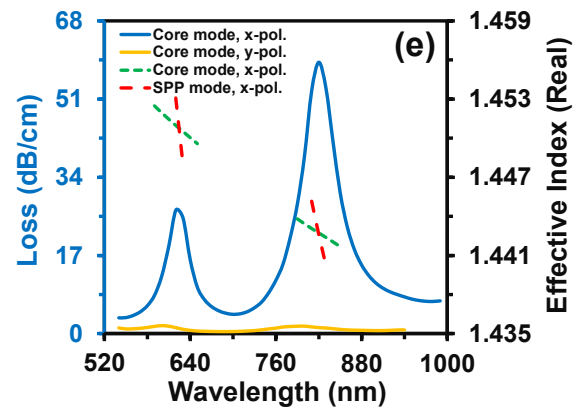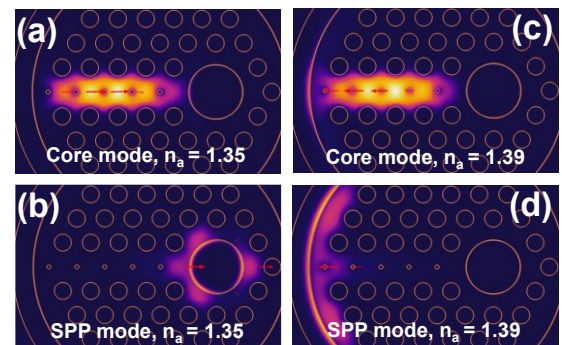

Fig. 3. Electric field distribution of core-guided mode and SPP mode for sensing scheme-I (a, b) at n_a=1.35, (c, d) n_a=1.39, respectively, (e) loss spectrum and phase-matching condition at n_a=1.35 and 1.39.
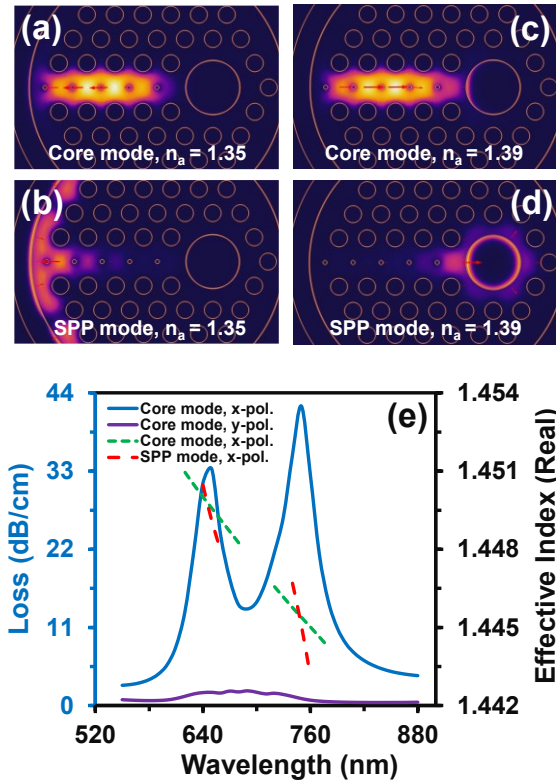
External cannel RI < Internal Channel RI

Fig. 4. Electric field distribution for sensing scheme-II (a, b) at n_a=1.35, (c, d) at n_a=1.39, respectively, (e) loss spectrum and phase-matching condition at n_a=1.35 and 1.39.

Figs. 3(a, c) and 3(b, d) demonstrate the core-guided modes and SPP modes for analyte RI of 1.35 in the internal channel and RI 1.39 in the external channel for sensing scheme-I. The core and SPP modes exhibit strong coupling intensity in the *x*-polarized mode then *y*-polarized mode which is more evident in Fig. 3(e). Figs. 4(a, c) and 4(b, d) exhibit the core-guided and SPP modes for sensing scheme-II with analyte RI of 1.35 and RI 1.39 in the external and internal channels, respectively. In Scheme-II also, the *x*-polarized mode exhibits strong coupling intensity than the *y*-polarized mode (see Fig. 4(e)). Fig. 5 represents the sensing performances for the sensing scheme-I. Fig. 5(a) depicts the propagation loss spectrums when the analyte RI of the external channel is kept constant at 1.40 and analyte RI is varied from 1.33 to 1.36 in the internal channel (Case I). Observing that the hybrid sensor exhibits the maximum WS of 2,000 nm/RIU. The WS of the hybrid sensor is calculated using the equation [15],

$$R(RIU) = \Delta n_a \times \Delta\lambda_{min} / \Delta\lambda_{peak} \qquad (4)$$

where S_λ indicates the wavelength sensitivity in *nm/RIU*, Δn_a defines the variation of analyte RI in RIU, $\Delta\lambda_{peak}$ defines the resonance wavelength shift in nm. Fig. 5(b) shows the loss spectrums for the changing of external channel analyte RI from 1.37 to 1.40 and internal channel analyte RI is fixed at 1.33 (Case II). In case II, maximum WS of 12,000 nm/RIU is exhibited by the hybrid sensor.

TABLE I
SENSOR PERFORMANCE FOR THE SCHEME- I

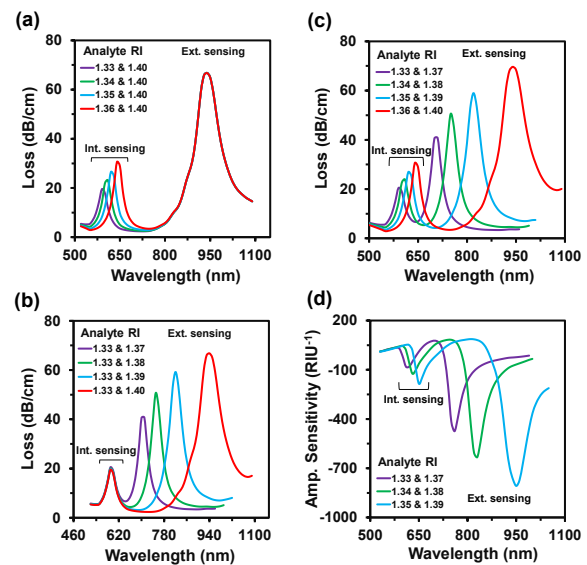| Ref. Ch.	Analyte RI	Maximum wav. sens. (nm/RIU)	Maximum wav. res. (RIU)	Amp sens. (RIU⁻¹)	FOM (RIU⁻¹)
Internal Channel	1.33	2,000	5×10^{-4}	80	43
	1.34	1,000	1×10^{-4}	124	23
	1.35	2,000	5×10^{-5}	185	47
	1.36	N/A	N/A	N/A	N/A
External Channel	1.37	4,000	2.5×10^{-5}	474	87
	1.38	7,000	1.4×10^{-5}	633	146
	1.39	12,000	8.33×10^{-6}	807	200
	1.40	N/A	N/A	N/A	N/A

Fig. 5. Loss spectrum for the sensing scheme-I. (a) RI is varied from 1.33 to 1.36 in the internal channel and RI is 1.40 for the external channel (case I), (b) RI is varied from 1.37 to 1.40 in the external channel and keep fixed n_a=1.33 in the internal channel (case II), (c) simultaneously analyte RI variation in both channels i.e. from 1.33 to 1.36 in the internal and 1.37 to 1.40 in the external channel (case III), (d) amplitude sensitivity a function of wavelength in case III.

Fig. 5(c) illustrates the loss spectrums for the simultaneous variation of analyte RI from 1.33 to 1.36 in the internal channel and from 1.37 to 1.40 in the external channel (Case III). From Figs. 5(a-c), it seems that each analyte RI have a fixed resonant wavelength and peak loss which is the same in the case I to III (see table 1). The amplitude sensitivities (AS) of case III presented in Fig. 5(d) where maximum AS of 807 RIU⁻¹ in the analyte RI range of 1.33 to 1.40. In general, the AS of a sensor will be high with increasing analyte RI and calculated by the following equation [34];

$$S_A(\lambda)[RIU^{-1}] = -\frac{1}{\alpha(\lambda,n_a)}\frac{\partial\alpha(\lambda,n_a)}{\partial n_a} \qquad (5)$$

where $\alpha(\lambda\ n_a)$ is the confinement loss at any analyte RI, and $\delta\alpha(\lambda\ n_a)$ is the difference between two-loss spectra.
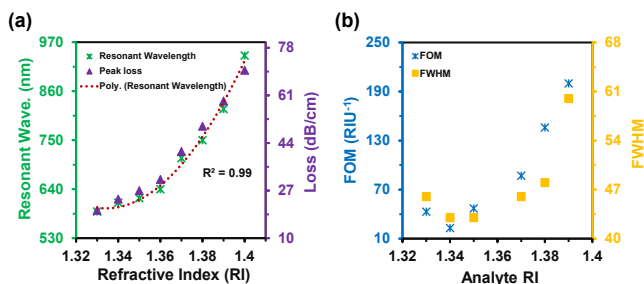
(a)

(b)

Fig. 6. (a) Polynomial curve fitting, and (b) FOM and FWHM for different analyte RI.

From Table 1, it is found that there is no significant change in the WSs while varied the analyte RI either in one channel or both channels. Polynomial curve fitting of resonant wavelengths and confinement loss of the sensor are shown in Fig. 6(a) where the R^2 is 0.99 that indicates excellent sensing response. Fig. 6(b) represents the figure of merits (FOM) (WS/ Full-width at Half Maximum (FWHM)) and a maximum FOM value of 200 RIU^{-1} is obtained at the analyte RI 1.39. The FOM also indicates the output efficiency of a sensor. Therefore, FOM should be high which leads to being considered the sensor highly effective. A similar performance analysis like Scheme-I has been carried out for Scheme-II as well and shown in Fig. 7. In Scheme-II, higher RI values are considered for internal channel and lower RI values for external channel to investigate the performance dependency on the channels. Fig. 7(a) displays the loss spectrum while analyte RI is shifting forward from 1.33 to 1.37 for the external channel and RI is fixed at 1.40 for the internal channel. The hybrid sensor exhibits the highest WS of 3,000 nm/RIU (see Table 2) for the external channel RI variation.
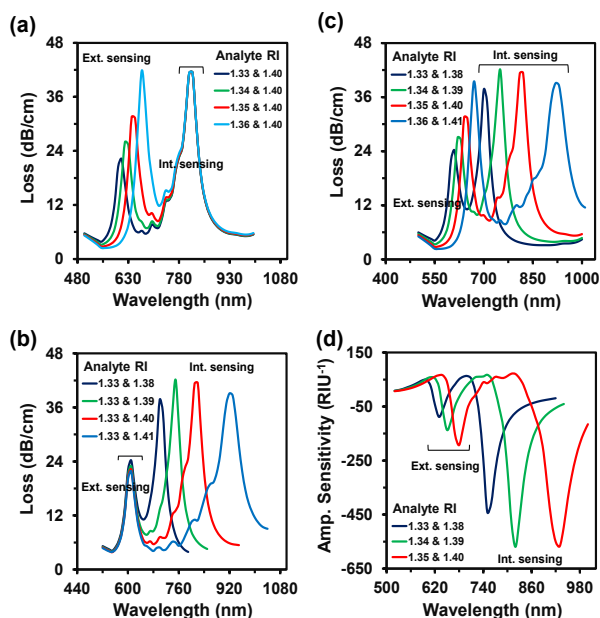
(a)

(c)

(b)

(d)

Fig. 7. Loss spectrum for the Scheme-II while RI is changing (a) from 1.33 to 1.36 in the internal channel and (b) from the 1.37 to 1.40 in the external channel, (c) analyte RI variation in both internal (from 1.33 to 1.36) and external (from 1.37 to 1.40) channels simultaneously, (d) AS spectrums for simultaneous analyte RI variation in both channels.

TABLE II
SENSOR PERFORMANCE FOR THE SCHEME- II

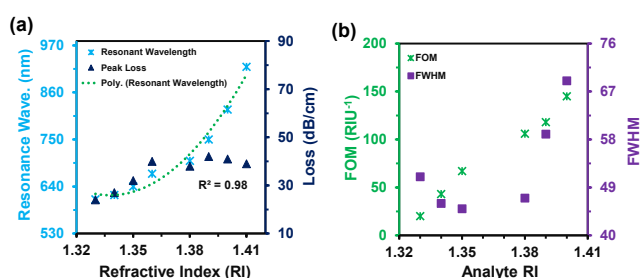| Ref. Ch.	Analyte RI	Maximum wav. sens. (nm/RIU)	Maximum wav. res. (RIU)	Amp. sens. (RIU^{-1})	FOM (RIU^{-1})
External Channel	1.33	1,000	1×10^{-4}	88	20
	1.34	2,000	5×10^{-4}	137	43
	1.35	3,000	3.3×10^{-5}	193	67
	1.36	N/A	N/A	N/A	N/A
Internal Channel	1.38	5,000	2.0×10^{-5}	440	106
	1.39	7,000	1.4×10^{-5}	569	118
	1.40	10,000	1.0×10^{-5}	567	145
	1.41	N/A	N/A	N/A	N/A

(a)

(b)

Fig. 8. For Scheme-II, (a) Polynomial curve fitting, and (b) the correlation of FOM and FWHM as a function of analyte RI variations.

The effect on the loss spectrum for analytes RI variation from 1.38 to 1.40 in the internal channel is shown in Fig. 7(b) and depicts the maximum WS of 10,000 nm/RIU. Fig. 7(c) displays the spectrums for concurrently analyte RI forward shifting for Scheme-II. In Scheme-II, the hybrid sensor exhibits the highest WS of 10,000 nm/RIU and AS of 569 RIU^{-1} in the sensing range of 1.33 to 1.41 (see Fig. 7(d)). It is noticeable that sensor performances are almost the same when analytes RI are varied in one channel or both channels together. Fig. 8(a) displays the polynomial cure fitting where the R^2 value is 0.98 and maximum FOM of 145 RIU^{-1} (see Fig. 4(b)) for the Scheme-II. Comparing the sensing scheme-I and II, the performance of the sensor is better for sensing scheme-I in terms of maximum WS (i.e., 12,000 nm/RIU), AS (8047 RIU^{-1}), resolution (i.e., 8.33×10^{-6} RIU), and FOM (i.e., 200 RIU^{-1}).

IV. FIBER CORE AND FABRICATION TOLERANCE ANALYSIS

The proposed fiber core has significant effect on light transmission and excitation on the sensing channels. As fiber core is made by scaled-down air holes, the effect of the scaled-down air-holes on light propagation are investigated as shown in Fig. 9, while both of the channels are infiltrated with analyte RI of 1.38. In Fig. 9a(i), the scaled-down air holes are omitted to make a solid core. Therefore, external sensing channel absorbs more light and shows high confinement loss, 53 dB/cm with strong coupling intensity (see Figs. 9a(ii, iii))
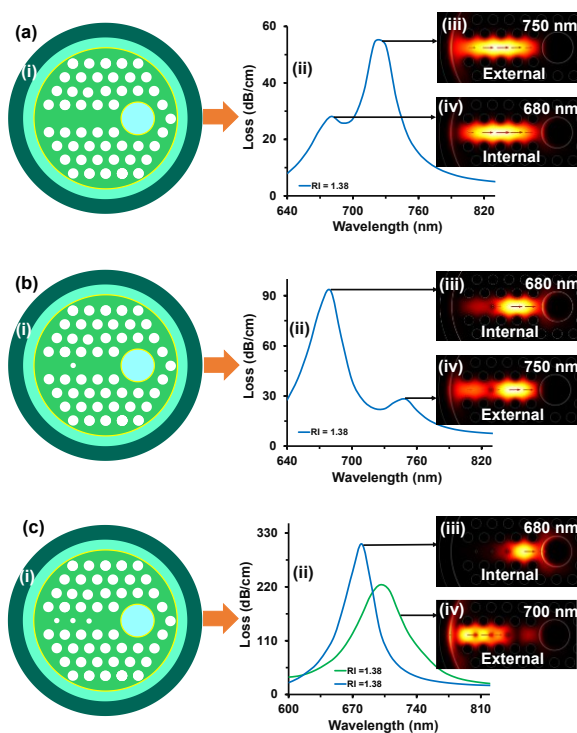
Fig. 9: Effect of scaled-down air holes in light distribution. Confinement loss and core-mode field distribution while both channels are filled with analyte RI 1.38. a(i-iv) Omitted all scaled-down air holes. b(i-iv) kept one scaled-down air-hole and omitted two from both sides, and c(i-iv) kept three scaled-down air-holes and omitted one from both sides.

compared to the internal sensing channel (loss depth 28 dB/cm, see Fig. 9a(ii, iv)). In addition, the resonant wavelengths appear at 680 nm and 750 nm for internal and external sensing channels, respectively. Later, one scaled-down air hole is kept and omitted two scaled-down air holes from both sides (see Fig. 9 b(i)). The sensor shows high loss depth (93 dB/cm) with strong coupling intensity (see Figs. 9b(ii, iii)) in internal sensing channel compared to the external sensing channel (loss depth 28 dB/cm, see Figs. 9b(ii, iv)). However, the resonant wavelengths are appeared at the same wavelengths as like Fig. 9a(ii). Finally, three scaled-down air holes are kept in the centre and one scaled-down air hole is omitted from both sides (see Fig. 9c(i)). In this case, the sensor shows completely different response compared to Figs.9a(ii) and b(ii) and exhibits separate loss spectrums for both channels. Also, the sensor shows high confinement losses of 308 dB/cm and 224 dB/cm at the resonant wavelengths of 680 nm and 700 nm, respectively for the internal and external channels (see Figs. 9c(ii-iv)). The high confinement loss limits the fiber length and difficult to measure in practice because of generating immeasurable sensing signal in the output system as it disappears immediately after lunching the incident light. However, five scaled-down air holes are considered to make light transmitting core in the hybrid sensor (See Fig. 2a(i)). The sensor's resonant wavelength appears at 700 nm for internal and 750 nm for external sensing channel respectively for analyte RI 1.38 (See Fig. 2 a(ii)). Also, it is noticeable that the confinement losses are almost same 50 dB/cm and 52 dB/cm for internal and external channels, respectively. Also,

the coupling intensity of both channels are almost same (Figs. 2a(iii, iv). Form the above discussions, we can say that by using different core arrangements, we can strongly excite only one channel at a time which will limit the multi-analyte detection capabilities. To excite both sensing channels at the same time with almost similar coupling strength, our proposed optimized five scaled-down air-hole core is more suitable.

Fabrication tolerance of the introduced hybrid sensor has been examined by considering an analyte RI of 1.33 for both channels. The t_g (gold layer thickness) is varied from 30 to 50 nm shown in Fig. 10(a). The resonant peak shifts from 580 nm to 600 nm with the rise of t_g from 30 to 40 nm. The resonant peak shift is highest at t_g=40 nm. Also, the maximum AS of 120 RIU^{-1} exhibits at t_g = 40 nm (see Fig. 10(b)), as a result, t_g=40 nm is considered as optimum. The loss spectrums for the change of pitch size (Λ) are shown in Fig. 11(a). According to Fig. 11(a), changing of Λ values has not shown any significant effect in the shift of resonant peak (only 10 nm) and confinement loss (only 2 dB/cm). Similar scenarios are observed for the variation of d_1 (see Fig. 11(b)) and d_2 (see Fig. 11(c)). It seems that peak confinement losses vary slightly for ± 10% change in diameters from the optimum values of d_1=1.4 and d_2=0.35 μm, however, the resonant peaks remain the same (600 nm). Therefore, d_1=1.4 and d_2=0.35 μm are considered the optimum diameter of regular air-holes and scaled-down air holes, respectively. The effect of large air hole diameter (d_3) modification is shown in Fig. 11(d). The confinement loss significantly increases with the rise of d_3 and resonant wavelength remains unchanged (600nm). Considering the signal-to-noise ratio and practical feasibility, the d_3 value is optimized to 4.4 μm for the internal channel diameter. However, the performance of the hybrid sensor is compared in Table 2. It is visible that few reported sensors also can detect two analytes, but performances are too low. In addition, only wavelength sensitivity and sensor resolution are mentioned for most of the sensors as an important performance measurement parameter. In Table 2, two sensors [18, 24] have been reported with 4 channels that can sense in a very short analyte RI range and shown maximum wavelength sensitivity of 4,600 nm/RIU and resolution of 2.17×10^{-5} RIU [18]. Furthermore, the rest of the reported works have been reported with 2 channels and shown the maximum WS and the resolution of 4,400 nm/RIU and 2.27×10^{-5} RIU, respectively [35]. Moreover, the maximum AS of 341 RIU^{-1} [36].
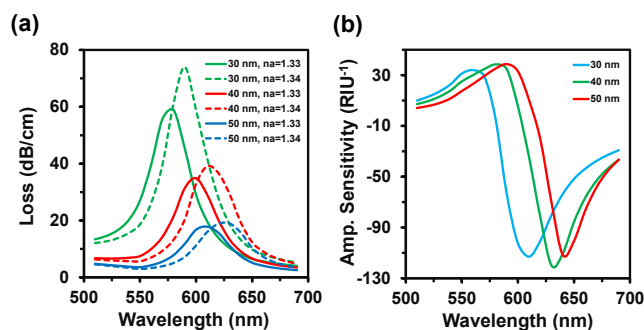

Fig. 10. Fabrication tolerance investigation of the sensor where (a) t_g thickness variation, (b) Amplitude sensitivity of t_g variation.

TABLE III
PROPOSED HYBRID SENSOR PERFORMANCE COMPARISON WITH REPORTED SENSOR

Structure type	Number of channels	Number of analytes	Materials	Detected RI range	Wavelength sensitivity (nm/RIU)	Wavelength resolution (RIU)	Amplitude sensitivity (RIU^{-1})	Ref.
PCF based SPR sensor for multianalyte sensing	2 Channels	2 Analytes	Au	1.30-1.40	1000 3750	1.00×10^{-4} 2.67×10^{-5}	N/A	[17]
Double D-shaped PCF based SPR biosensor	4 Channels	2 Analytes	Au Ag	1.33 -1.366	2500 3083	4.0×10^{-5} 3.2×10^{-5}	N/A	[24]
Microfluidic slot-based PCF biosensor	4 Channels	2 Analytes	Au, T_2O_5	1.33-1.36	4600 2300	2.17×10^{-5} 4.35×10^{-5}	N/A	[18]
Duale channel central hole based PCF sensor	2 Channels	2 Analytes	Au	1.40 - 1.41	4400 3500	2.27×10^{-5} 2.86×10^{-5}	N/A	[35]
Optical fiber based SPR sensor	2 Channels	1 Analytes	GNP Au/ITO	1.3666-1.3683	1963	5.09×10^{-5}	334.1	[36]
Wagon wheel fiber based plasmonic sensor	3 Channels	2 Analytes	Au	1.33-1.46	1535 1550	6.5×10^{-5} 6.5×10^{-5}	N/A	[37]
Optical fiber based dual channel biosensor	2 Channels	2 Analytes	Ag, Au, ITO	1.525 -1.578	1951 2496	$5.1\times10^{-}$ 4.0×10^{-5}	N/A	[38]
Hybrid PCF based SPR sensor	2 Channels	2 Analytes	Au	1.33-1.40 1.33-1.39	12,000 10,000	8.33×10^{-6} 1.0×10^{-5}	807 569	This work

Besides, the proposed hybrid sensor has two analyte channels and can detect two different analytes simultaneously with high wavelength and amplitude sensitivities of 12,000 nm/RIU and 807 RIU^{-1}, respectively. From the above discussion, it can be said that the introduced hybrid sensor is able to detect multi-analyte simultaneously. Also, the proposed sensor is not limited to detect multi-analyte only, possible to detect single analyte with high sensing accuracy.

Fig. 11. Fabrication tolerance investigation of the sensor parameters where (c) Λ, (d) d_1, (e) d_2, and (f) d_3 display the loss spectrum effects.

I. CONCLUSION

In summary, multi-analyte detection through a hybrid sensor is proposed by combining the internal and external sensing approaches. The sensing performance is numerically investigated to demonstrate the multi-analyte detection capability of the sensor. The proposed hybrid sensor shows the maximum WS of 12,000 nm/RIU, with the resolution of 8.33×10^{-6} RIU in the external channel whereas maximum WS is 10,000 nm/RIU with the resolution of 1×10^{-5} RIU in the internal channel. A high AS of 807 RIU^{-1} and 569 RIU^{-1} are obtained in the external and internal channels, respectively. Furthermore, the sensor shows good FOM values of 200 RIU^{-1} and 145 RIU^{-1} for the external and internal channels, respectively. Therefore, due to the high biosensing performance with multi-analyte detection capability, the proposed hybrid approach will be a potential candidate for POC application in detecting viruses, glucose, proteins and DNA/RNA, etc.

Disclosures. The authors declare no conflicts of interest.

References:

[1] N. Ayyanar, K. Sreekanth, G. T. Raja, and M. M. Rajan, "Photonic Crystal Fiber Based Reconfigurable Biosensor Using Phase Change Material," *IEEE Trans. Nanobioscience,* 2021.
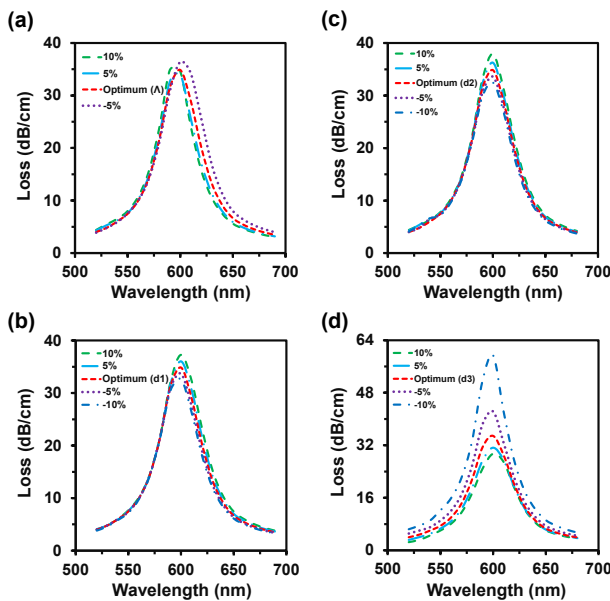
[2] F. Haider, R. A. Aoni, R. Ahmed, G. A. Mahdiraji, M. F. Azman, and F. R. M. Adikan, "Mode-multiplex plasmonic sensor for multi-analyte detection," *Opt. Lett.,* vol. 45, no. 14, pp. 3945-3948, 2020.

[3] A. Gandhi, K. Senthilnathan, P. Ramesh Babu, and Q. Li, "Highly Sensitive Localized Surface Plasmon Polariton Based D-Type Twin-Hole Photonic Crystal Fiber Microbiosensor: Enhanced Scheme for SERS Reinforcement," *Sensors,* vol. 20, no. 18, p. 5248, 2020.

[4] J. Li, H. Qu, Z. Li, K. Nallappan, D. Liu, and J. Wang, "A Review: Development of Fiber-Optic Platforms for Refractive Index Sensing Applications," *Sensors and Actuators Reports,* p. 100018, 2020.

[5] S. Zeng *et al.*, "Graphene–gold metasurface architectures for ultrasensitive plasmonic biosensing," *Adv. Mater.,* vol. 27, no. 40, pp. 6163-6169, 2015.

[6] J. Wang, L. Pei, L. Wu, J. Wang, Z. Ruan, and J. Zheng, "A polarization-independent SPR sensor based on photonic crystal fiber for low RI detection," *Plasmonics,* vol. 15, no. 2, pp. 327-333, 2020.

[7] C. Liu *et al.*, "Birefringent PCF-based SPR sensor for a broad range of low refractive index detection," *IEEE Photon. Technol. Lett.,* vol. 30, no. 16, pp. 1471-1474, 2018.

[8] E. Haque, A. Al Noman, M. A. Hossain, N. H. Hai, Y. Namihira, and F. Ahmed, "Highly Sensitive D-Shaped Plasmonic Refractive Index Sensor for a Broad Range of Refractive Index Detection," *IEEE Photon. J.,* vol. 13, no. 1, pp. 1-11, 2021.

[9] H. Fang *et al.*, "Research on photonic crystal fiber based on a surface plasmon resonance sensor with segmented silver-titanium dioxide film," *JOSA B,* vol. 37, no. 3, pp. 736-744, 2020.

[10] Y. Jia, Z. Li, H. Wang, M. Saeed, and H. Cai, "Sensitivity Enhancement of a Surface Plasmon Resonance Sensor with Platinum Diselenide," *Sensors,* vol. 20, no. 1, p. 131, 2020.

[11] F. Wu *et al.*, "Ultrasensitive and rapid detection of malaria using graphene-enhanced surface plasmon resonance," *2D Materials,* vol. 7, no. 4, p. 045019, 2020.

[12] F. Haider, R. A. Aoni, R. Ahmed, W. J. Chew, and G. A. Mahdiraji, "Alphabetic-Core Assisted Microstructure Fiber Based Plasmonic Biosensor," *Plasmonics,* pp. 1-10, 2020.

[13] J. N. Dash and R. Jha, "SPR biosensor based on polymer PCF coated with conducting metal oxide," *IEEE Photon. Technol. Lett,* vol. 26, no. 6, pp. 595-598, 2014.

[14] M. M. R. N. Jahan, Mominul Ahsan, Md. Abdul Based, M. M. Rana, and Saravanakumar Gurusamy, "Photonic Crystal Fiber Based Biosensor for Pseudomonas Bacteria Detection: A Simulation Study," *IEEE Access,* vol. vol. 9, pp. pp. 42206-42215, 2021.

[15] A. Yasli, H. Ademgil, S. Haxha, and A. Aggoun, "Multi-Channel Photonic Crystal Fiber Based Surface Plasmon Resonance Sensor for Multi-Analyte Sensing," *IEEE Photon. J.,* vol. 12, no. 1, pp. 1-15, 2019.

[16] S. Chu *et al.*, "A Surface Plasmon Resonance Bio-Sensor based on Dual Core D-Shaped Photonic Crystal Fibre Embedded with Silver Nanowires for Multi-Sensing," *IEEE Sens. J.,* 2020.

[17] V. Kaur and S. Singh, "A dual-channel surface plasmon resonance biosensor based on a photonic crystal fiber for multianalyte sensing," *J. Comput. Electron.,* pp. 1-10, 2019.

[18] R. Otupiri, E. K. Akowuah, and S. Haxha, "Multi-channel SPR biosensor based on PCF for multi-analyte sensing applications," *Opt. Express,* vol. 23, no. 12, pp. 15716-15727, 2015.

[19] N. D. Gómez-Cardona, E. Reyes-Vera, and P. Torres, "Multi-plasmon resonances in microstructured optical fibers: Extending the detection range of SPR sensors and a multi-analyte sensing technique," *IEEE Sens. J.,* vol. 18, no. 18, pp. 7492-7498, 2018.

[20] P. Bing *et al.*, "Analysis of Dual-Channel Simultaneous Detection of Photonic Crystal Fiber Sensors," *Plasmonics,* pp. 1-6, 2020.

[21] Y. Wang, Q. Huang, W. Zhu, M. Yang, and E. Lewis, "Novel optical fiber SPR temperature sensor based on MMF-PCF-MMF structure and gold-PDMS film: erratum," *Opt. Express,* vol. 27, no. 8, pp. 10813-10813, 2019.

[22] C. Zhou *et al.*, "D-Shaped Photonic Crystal Fiber Plasmon Sensors Based on Self-Reference Channel," *IEEE Photon. Technol. Lett.,* vol. 32, no. 10, pp. 589-591, 2020.

[23] F. Haider, R. A. Aoni, R. Ahmed, M. S. Islam, and A. E. Miroshnichenko, "Propagation controlled photonic crystal fiber-based plasmonic sensor via scaled-down approach," *IEEE Sens. J.,* vol. 19, no. 3, pp. 962-969, 2018.

[24] A. Yasli, H. Ademgil, S. Haxha, and A. Aggoun, "Multi-Channel Photonic Crystal Fiber based Surface Plasmon Resonance Sensor for Multi-Analyte Sensing," *IEEE Photon. J.,* 2019.

[25] M. F. Azman, G. A. Mahdiraji, W. R. Wong, R. A. Aoni, and F. R. M. Adikan, "Design and fabrication of copper-filled photonic crystal fiber based polarization filters," *Appl. Opt.,* vol. 58, no. 8, pp. 2068-2075, 2019.

[26] G. Amouzad Mahdiraji *et al.*, "Challenges and solutions in fabrication of silica-based photonic crystal fibers: an experimental study," *Opt. Fiber Technol.,* vol. 33, no. 1-2, pp. 85-104, 2014.

[27] M. Mashrafi, Q. Kamrunnahar, F. Haider, R. Haider, R. A. Aoni, and R. Ahmed, "Bio-inspired butterfly core-shaped photonic crystal fiber-based refractive index sensor," *OSA Continuum,* vol. 4, no. 4, pp. 1179-1190, 2021.

[28] I. Danlard and E. K. Akowuah, "Assaying with PCF-based SPR refractive index biosensors: From recent configurations to outstanding detection limits," *Opt. Fiber Technol,* vol. 54, p. 102083, 2020.

[29] M. Al Mahfuz, M. A. Hossain, E. Haque, N. H. Hai, Y. Namihira, and F. Ahmed, "Dual-core photonic crystal fiber-based plasmonic RI sensor in the visible to near-IR operating band," *IEEE Sens. J.,* vol. 20, no. 14, pp. 7692-7700, 2020.

[30] Z. Vafapour, "Polarization-independent perfect optical metamaterial absorber as a glucose sensor in Food Industry applications," *IEEE Trans. Nanobioscience,* vol. 18, no. 4, pp. 622-627, 2019.

[31] P. Y. Liu *et al.*, "Cell refractive index for cell biology and disease diagnosis: past, present and future," *Lab on a Chip,* vol. 16, no. 4, pp. 634-644, 2016.

[32] U. Dinish, G. Balasundaram, Y. T. Chang, and M. Olivo, "Sensitive multiplex detection of serological liver cancer biomarkers using SERS-active photonic crystal fiber probe," *Journal of biophotonics,* vol. 7, no. 11-12, pp. 956-965, 2014.

[33] X. Kong *et al.*, "Chemical and biological sensing using diatom photonic crystal biosilica with in-situ growth plasmonic nanoparticles," *IEEE Trans. Nanobioscience,* vol. 15, no. 8, pp. 828-834, 2016.

[34] M. R. Hasan *et al.*, "Spiral photonic crystal fiber-based dual-polarized surface plasmon resonance biosensor," *IEEE Sens. J.,* vol. 18, no. 1, pp. 133-140, 2018.

[35] L. Xia, B. Shuai, W. Li, and D. Liu, "Polarization detection analysis of dual-channel surface plasmon resonance sensing for silicone oils based on the D-shaped fiber with a central hole," *Opt. Commun.,* vol. 285, no. 18, pp. 3730-3734, 2012.

[36] Y. Chen, Q. Xie, X. Li, H. Zhou, X. Hong, and Y. Geng, "Experimental realization of D-shaped photonic crystal fiber SPR sensor," *J. Phys. D Appl. Phys.,* vol. 50, no. 2, p. 025101, 2016.

[37] Y. Zhang, C. Zhou, L. Xia, X. Yu, and D. Liu, "Wagon wheel fiber based multichannel plasmonic sensor," *Opt. Express,* vol. 19, no. 23, pp. 22863-22873, 2011.

[38] M. Lu *et al.*, "Dual channel multilayer-coated surface plasmon resonance sensor for dual refractive index range measurements," *Opt. Express,* vol. 25, no. 8, pp. 8563-8570, 2017.